RSC Advances

PAPER

View Article Online
View Journal | View Issue

Cite this: *RSC Adv.*, 2024, **14**, 39927

The corrosion resistance of white ultra-high performance concrete under the coupling environment of acid rain and carbonization

Huiying Hu,[a] Rui Ma,[ab] Ziyang Tian,[a] Zhidan Rong*[c] and Daosheng Sun[a]

Acid rain and carbonization are two primary types of environmental corrosion that threaten the health of urban concrete structures over time. However, the coupling effects of acid rain and carbonization on concrete deterioration have been rarely reported. In this paper, four coupling regimes were designed using accelerated simulation experiments to investigate the deterioration properties of white ultra-high performance concrete (WUHPC). The results showed that under acid rain corrosion, the WUHPC surface was covered with white crystals before peeling off after 7 days, resulting first in an increase, followed by a rapid decrease in weight and strength, and the erosion depth linearly increased at a rate of 33.0 μm per day. Meanwhile, negligible changes occurred with only carbonization. However, under coupling corrosion, the deterioration worsened after environmental alternation. The strength of WUHPC with acid rain after carbonization decreased by 27.7%, reaching a minimum of 72.0 MPa. The erosion depth growth under acid rain followed by carbonization was 20.0 μm per day, which was much faster than that (3.9 μm per day) of single carbonization. The major corrosion products under acid rain were gypsum crystal, and the crystal shrank with time, leaving more voids and a weakened bonding strength. The calcium carbonate sediment generated during carbonization blocked the pores on the surface, hindered the diffusion of acid solution, and partly consumed acid ions *via* dissolution, resulting in facilitated acid rain corrosion. Once carbonate was consumed in a short time, more capillary pores were unblocked to promote further acid rain corrosion.

Received 14th September 2024
Accepted 6th December 2024

DOI: 10.1039/d4ra06637e

rsc.li/rsc-advances

1 Introduction

With the rapid industrial development, large amounts of acid ions and CO_2 have been emitted into the atmosphere, causing the growing air pollution. It has been reported that the average pH of rainfall in China is 5.6,[1] and the average annual carbon dioxide concentration has reached a new record of 414.7 parts per million.[2] Acid rain and carbonization are two atmospheric contaminants causing global problems, including soil acidification, ecosystem destruction and building deterioration.[3–5] For urbanization, the demands for concrete constructions increase every year. Acid rain and carbonization have become the primary risks that cause durability problems for urban concretes,[6,7] resulting in frequent maintenance and shorter service lives than their designed age.[8,9] Acid rain contains many corrosive ions, for instance, SO_4^{2+}, H^+, and NH_4^+,[10] which react physically and chemically with hydration products, dissolve Ca^{2+} and destroy the microstructure of concrete, resulting in decreased concrete strength, crack formation and, finally, structural failure.[6,11–15] Moreover, sulfate and acid ions in acid rain break the protective layer and increase the risk of steel rebar corrosion in concrete.[16–19] Carbonization consumes $Ca(OH)_2$ in concrete and decreases the pH value, damaging the microstructure and causing shrinkage and cracking of concrete.[20] Therefore, global efforts have been undertaken toward low-carbon developments to repair the ecological environment for human survival. Because the production of concrete requires considerable energy and produces significant CO_2 emission, it is urgent to increase the service life of concrete to decrease the environmental impacts in their full-life cycle.[21–23] Thus, how to improve the corrosion resistance of concrete is a critical problem to address for low carbon development in the construction industry.[24]

Numerous studies have been reported on the corrosion of acid rain and carbonization on concrete in the last two decades.[7,25,26] It was proved that acid rain corrosion on concrete is a complex process, and can be divided into acid erosion and sulfate erosion.[27] For acid erosion, H^+ reacts with hydrated calcium hydroxide and calcium aluminate in concrete to form soluble products, which destroys the structure and further promotes the hydrolysis reaction.[28,29] A sulfate attack is more

[a]College of Materials and Chemical Engineering, Anhui Jianzhu University, Hefei, 230601, China. E-mail: marui@ahjzu.edu.cn
[b]College of Civil and Environmental Engineering, National University of Singapore, 117578, Singapore
[c]Department of Materials Science and Engineering, Southeast University, Nanjing, 210023, China

complex with the formation and growth of gypsum, ettringite and thaumasite.[30] The large size of the gypsum crystal causes partial expansion and cracking in concrete. These cracks subsequently become the new channel for acid ion transmission to further accelerate the corrosion.[31–35] Wang *et al.*[36] considered that the harm of gypsum was greater than ettringite in concrete. However, some research studies claimed that the gypsum did not fully fill the pores for an obvious expansion.[37] Moreover, NH_4^+ in acid rain reacts with OH^-, reducing the internal pH value. NH_4^+ can also replace Ca in the C–S–H gel, which decreases the cementation of the C–S–H gel and leads to the weakening of the mechanical properties and durability.[38]

Carbonization is the reaction of CO_2 in the air with calcium hydroxide, which initially decreases the porosity by calcium carbonate sedimentation and increases the compressive strength of concrete.[39] However, the decreased pH of the pore solution results in the decomposition of some hydration products over time.[40] However, most of the above works only focused on the deterioration under individual acid rain or carbonation corrosion. Under real conditions, the concrete suffers multiple impacts, but studies on the coupling effects of the environment are still limited.[41,42] Peng *et al.*[43] studied the deterioration mechanism of concrete under the coupling of sulfate and carbon dioxide, and demonstrated that the coupling condition made the concrete more fragile. Thus, further investigations on the deterioration process of concrete under coupling acid rain and carbonization coupling corrosion are necessary to improve corrosion resistance under conditions that more closely match the actual environment.

White ultra-high performance concrete (WUHPC) is a new cement-based construction material that combines excellent mechanical properties and good aesthetics appearance.[44,45] WUHPC has a white smooth surface and more compacted matrix. Compared to normal concrete, WUHPC does not need a secondary coating of paint. Furthermore, the air and liquid permeability are only 1/4 to 1/5 of that for normal concrete, which avoids frequent maintenance and leads to long durability.[46,47] WUHPC can be used as the building material for exterior structures to improve the mechanical and durability properties, and satisfies the requirement of a thin-wall, ultra-high or light-weight design of urban constructions.[48] Although WUHPC exhibits the expected resistance on corrosion, some surface efflorescence occurs under corrosion environment, which significantly disturbs the appearance. Furthermore, the surface deterioration still occurs with long-term service.

In this paper, acid rain and carbonization alternant-accelerated experiments were designed as coupling corrosion regimes. The macroscopic properties of WUHPC under different coupling regimes were studied to reveal the deterioration process, and the corrosion products and micropore structures were also analyzed.

2 Material and methods

2.1 Preparation of WUHPC

P W52.5 White Portland Cement (WPC), white silica fume (WSF), metakaolin (MK) and limestone powder (LP) were selected as binder materials. Fine aggregate was river sand with the fineness modulus of 2.59. Polycarboxylate water reducing agent with a reducing rate of over 30% was used to improve the workability. The chemical composition of the binder materials is listed in Table 1. The particle size distribution of different powders is shown in Fig. 1.

The WPC was partly replaced by mineral admixtures to reduce the initial hydration heat and the CO_2 emission. The weight ratio of WPC : WSF : MK : LP = 10 : 1 : 3 : 6 for the control group, and the W/B ratio of WUHPC was 0.18. The details of the mix proportion of WUHPC are listed in Table 2.

For the mixing procedure, the powders (including binders and sand) were first dry-mixed for 2 min to ensure good dispersion. After that, water and the water reducer were added slowly during continuous stirring until a uniform slurry was formed. Lastly, steel fiber was added and the mixture was stirred for another 3 min. The slurry was then cast into a mold with the size of 40 × 40 × 160 mm^3, placed under a standard environment (20 ± 2 °C, RH > 95%) for 36 h to demold, and steam-cured at 85 °C for 3 days.

2.2 Coupling corrosion regime

To simulate the acid rain and carbonization corrosion process, a harsh environment was created to accelerate the degradation of WUHPC. For the experiment, sulfuric acid with a mass fraction of 95–98%, nitric acid with a concentration of 65–68%, and saturated ammonium sulfate solution were used to prepare the simulated acid rain solution. The concentration of SO_4^{2+} in the solution was controlled to 0.5 mol L^{-1}, and the molar ratio of $SO_4^{2+} : NO_3^- : NH_4^+$ was set at 2 : 1.5 : 1, with the initial pH of 0.88. Carbonization was controlled using the carbon dioxide concentration of 20 ± 3%, a temperature of 20 ± 2 °C, and humidity of 70 ± 5%.

Each minor cycle of acid rain or carbonization-accelerated experiment was 1 week in length, and denoted as S or T, respectively. A major experiment cycle would last for 4 weeks. In the acid rain corrosion, the specimens were immersed in the simulated solution for 2.5 days, dried at 45 °C for 1 day, and the

Table 1 Chemical composition of the binder materials (wt%)

Materials	CaO	SiO_2	Al_2O_3	Fe_2O_3	MgO	Na_2O	SO_3	L.O.L	Whiteness/%
WPC	67.09	18.09	2.25	0.27	4.49	0.3	4.33	2.48	88.5
WSF	0.29	91.83	0.48	0.4	0.33	0.1	0.97	0.13	92.97
MK	0.48	95.62	0.9	0.06	0.37	0.04	2.34	0.06	96.16
LP	99.36	0.22	0.02	0.03	0.28	—	0.01	7.16	97.52

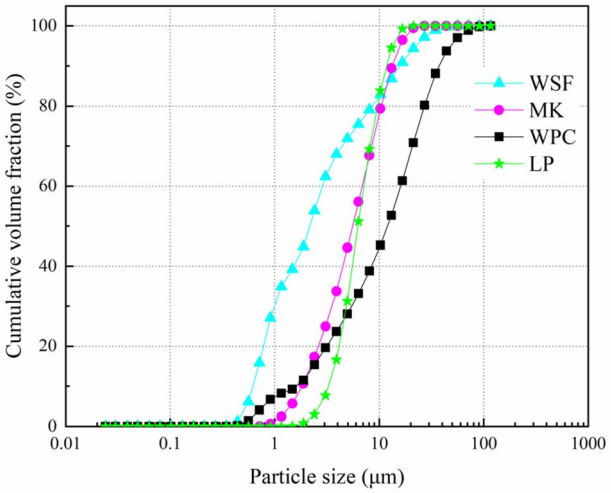

Fig. 1 Particle size distribution of the mixed binder materials.

process was repeated. The simulated solution was refreshed every 7 days. For carbonization, the specimens were sealed in a CO_2 ambient for 7 days. To compare the different corrosion processes, six corrosion regimes were determined: pure acid rain (4S); pure carbonization (4T); first acid rain for 3 weeks, followed by carbonation for 1 week, and repeated again (3S-T); first acid rain for 1 week, followed by carbonization for 3 weeks, and repeated again (S-3T); and the reversed processes denoted as 3T-S and T-3S. A schematic diagram of the whole experimental regime is presented in Fig. 2.

2.3 Test methods

2.3.1 Weight change ratio. The weights of the specimen before and after corrosion for each minor cycle were measured and recorded. Before being weighed, the specimen was dried at 45 °C until a constant mass was achieved. The weight change ratio was calculated following eqn (1), and an average was taken from three specimens for each group.

$$M = w_t - w_0 \times 100\%/m_0 \quad (1)$$

where M is the weight change ratio of WUHPC, and w_0 and w_t are the weights at the initial time and corroded after time t, respectively.

2.3.2 Compressive strength. The compressive strength of WUHPC was tested according to the Chinese standard "Strength test method for cement mortar" (GB/T 17671-2021). The specimens with the size of 40 × 40 × 160 mm^3 were compressed at a load of 2.4 ± 0.2 kN s^{-1}. The compressive strength of WUHPC was tested before and after major corrosion cycles with different regimes. For each group, three specimens were tested to make an average.

Table 2 The mix proportion of WUHPC (kg m^{-3})

WPC	SF	MK	LP	Sands	Water	WR	Fiber	Strength (MPa)	Whiteness (%)
500	50	150	300	1000	180	14	189	102.3	71.9

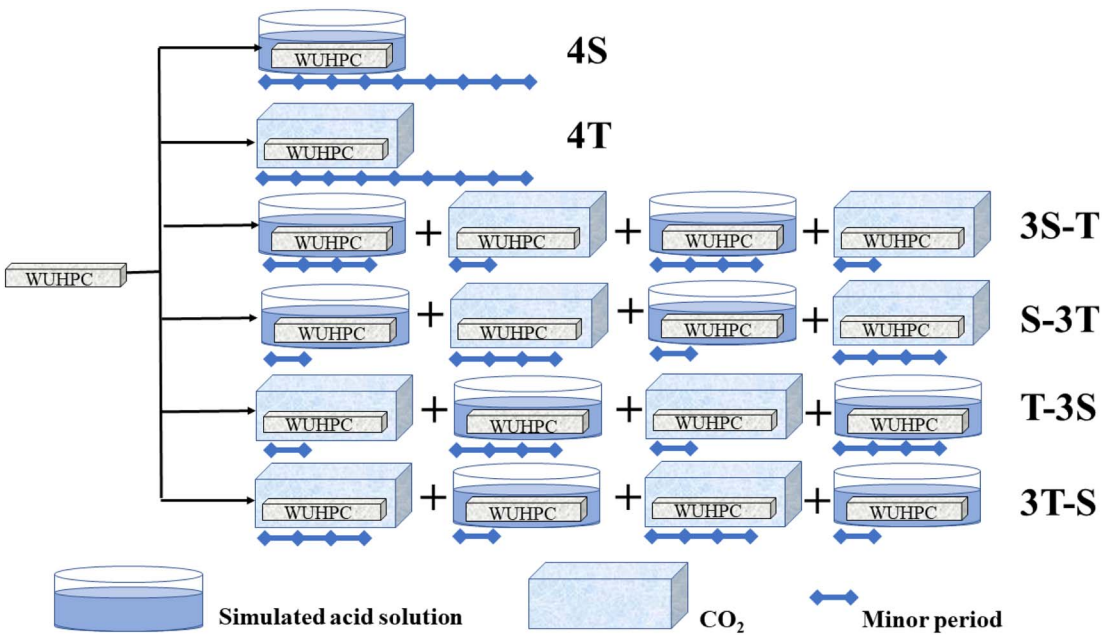

Fig. 2 Schematic of different coupling corrosion regimes.

2.3.3 Whiteness change rate. The whiteness of the WUHPC before and after corrosion was measured by a colorimeter. For each sample, three points at different positions on the surface were tested to obtain an average, and the whiteness change ratio was calculated by eqn (2).

$$W = W_t - W_1 \times 100\%/W_1 \quad (2)$$

where W is the change rate of the whiteness, and W_1 and W_t are the whiteness of WUHPC before and after corrosion at time t, respectively.

2.3.4 Erosion depth. Erosion depth is a common method to determine the degree of corrosion. Since the internal environment of the cement-based materials is alkaline, phenolphthalein is preferred as a color indicator to determine whether the specimen is corroded into neutral or acidic condition at the specific depth. In this test, the erosion depth was tested for every minor cycle under corrosion. The end of the specimen was cut into a slice with the thickness of 10 mm from the cross-section. Then, phenolphthalein solution was sprayed onto the cutting face. At last, a magnifying scope with a scale was used to observe the color change of the cutting face, and the width of the area that did not change into a mauve color was measured as the erosion depth. A schematic of the test process is shown in Fig. 3.

2.3.5 Corrosion products. X-ray diffraction (XRD) and thermogravimetry (TG) were used to analyze the component and content of the corrosion products by different regimes. The samples after corrosion were placed in anhydrous ethanol to stop hydration. Then, the corrosion products were ground into a powder and dried in a vacuum oven at 40 °C before testing. The sample was scanned in the 2θ range from 5°–80° during the XRD test, with the scanning rate of 10° min^{-1}. For the TG test, about 20 ± 0.5 mg sample was heated from 25 °C to 1000 °C at the rate of 10 °C min^{-1} under the N_2 atmosphere.

2.3.6 Pore size distribution. The pore structure was significantly affected by the corrosion process and determined the transmission of harmful ions. The pore structure was analyzed by low-field nuclear magnetic resonance (L-NMR) method. The relaxation time of ^1H from the water molecules in pores is related to the interaction between the water molecules and pore walls, and a longer relaxation time refers to a larger pore radius. The pore size distribution was detected by the transverse relaxation time distribution.[49] For sample preparation, WUHPC with the size of 2 × 2 × 10 mm^3 underwent vacuum water saturation for 7 days. The sample was then tested by NMR with the resonance frequency of 21.3 MHz, coil diameter of 60 mm and magnet temperature of 32 ± 0.02 °C.

2.3.7 Micro-morphology. The morphologies of the matrix and corrosion products were observed by scanning electron microscopy (SEM). To compare the morphology changes of the corrosion products under acid rain corrosion, the WUHPC specimens were soaked in acid rain solution for different designated times (1 h, 6 h, 18 h, 30 h, 54 h), and the hydration was stopped by ethyl alcohol. The samples were obtained from the surface area, and covered with Au film before observation.

3 Experiment results and analysis

3.1 Weight change

Fig. 4 shows the weight change of WUHPC under different corrosion paths. From the picture, the weight change in the pure carbonization process was negligible. Meanwhile, the weight of WUHPC under acid rain was increased by 1.42% during the first 7 days, and then began to decrease with a sudden accelerated ratio at the last half period. For the single acid rain process, the total weight lost was 3.32%, and about 70% happened during the last 21 days. However, during the coupling corrosion process, the total weight loss was smaller than a single one. The weight increase rate slightly decreased when the carbonization step was changed to acid rain at the first minor cycle. The weight of the sample undergoing carbonization, followed by acid rain, first increased and then decreased, displaying a more significant change. The weight increase of the S-3T and 3S-T samples in the first carbonation cycle was 0.24%

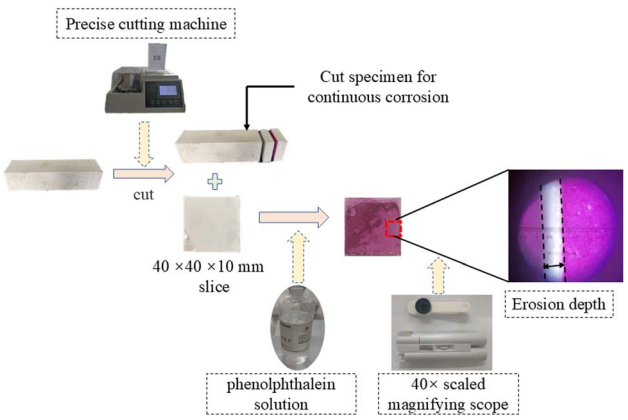

Fig. 3 Diagram of cutting and neutralization depth testing procedure.

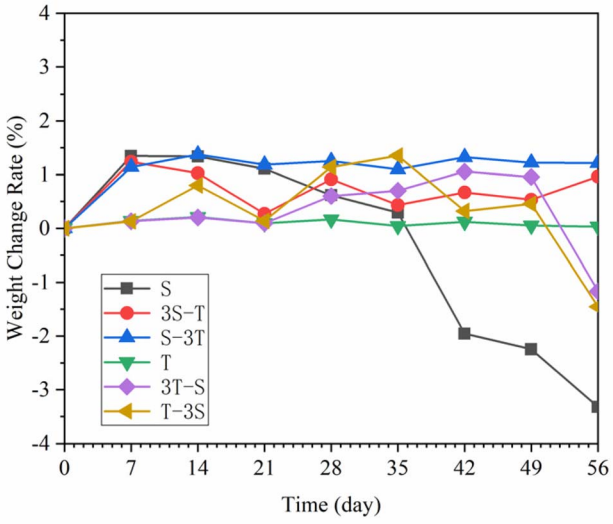

Fig. 4 Mass change rate of WUHPC under different paths.

and 0.65%, respectively. Also, for the T-3S and 3T-S regime, a high range weight loss occurred in the last acid rain cycles.

The weight change of WUHPC was dominated by the growth and exfoliation of the corrosion products. At the early age of acid corrosion, more white products were precipitated on the surface, causing the increase of weight. Then, these products began to peel off with time, resulting in the weight decline. For the coupling corrosion, the total acid rain time was shorter than that of the pure process, so the weight loss was less. However, the coupling corrosion induced more surface defects, especially by acid rain, and made the transmission of corrosion ions easier, which increased the weight change rate at the first alternate minor cycle. The results also proved that during the early part of the experiment, carbonization contributed toward resisting the formation of acid rain products, but this effect quickly decreased upon continuous corrosion.

3.2 Compressive strength

The variation of the compressive strength of WUHPC under different corrosion paths is shown in Fig. 5. It was observed that under single acid rain, the compressive strength increased by 11.7% in the first major cycle, and then decreased by 22.2% in the later one. Meanwhile, for carbonization, the strength first decreased by 12.7% and then became stable. However, with the coupling corrosion, only the samples under S-3T reached the minimum strength drop, which was 91.65 MPa with 8% loss. The samples under other regimes all showed greater decreases in strength. By comparison, it was found that the strength decreased more significantly than in the other cases, and reached 27.7% for acid rain followed by carbonation (T-3S, 3T-S).

From the results, the corrosion resistance of WUHPC was much better than that of normal concrete. The strength decrease under such severe conditions was less than 30%. Furthermore, the strength improvement in the early stages of the experiment was primarily contributed by the deposition of small corrosion products, such as calcium carbonate, which filled the pores and compacted the matrix. However, this effect was reversed if the products became larger and consumed more hydration products. Still, if the WUHPC was corroded by carbonation followed with acid rain, the precipitated products were dissolved with acid solution, promoting further corrosion and accelerated strength failure.

3.3 Surface appearance degradation

Fig. 6 presents the digital pictures of the surface appearance of WUHPC after corrosion, and the whiteness change is shown in Fig. 7. As shown in Fig. 6, the surface was smooth before corrosion, and slightly changed after carbonization. The whiteness of WUHPC was increased by about 8.2% at the first 7 days, then decreased with the continuing carbonization. At the early stage (7 days) of the acid rain corrosion, a large number of white crystals and bubbles were generated on the surface, which roughened the surface and significantly increased the whiteness by about 20.8%. As the time went on, the surface began to break from the corners, and the increase of whiteness became more constant. Under acid rain corrosion after carbonization, the surface of WUHPC was grayish white with generated white crystals and bubbles. Once samples underwent carbonization

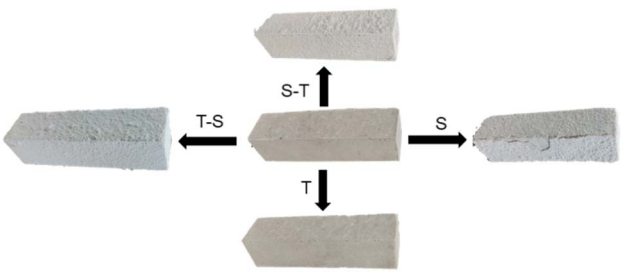

Fig. 6 Surface appearance of WUHPC after corrosion.

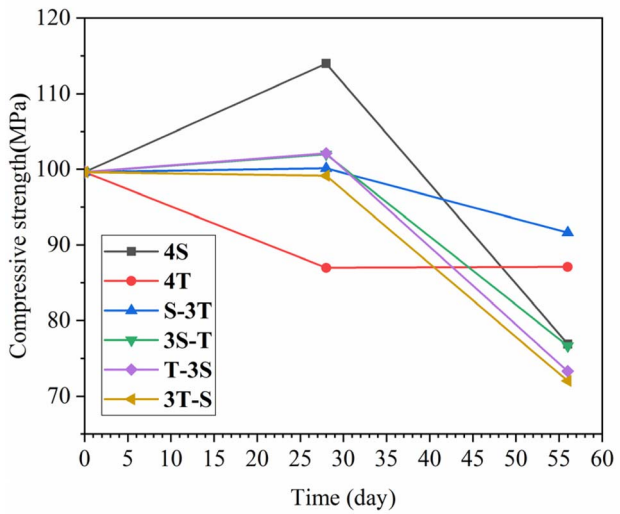

Fig. 5 Variation in WUHPC compressive strength under different paths.

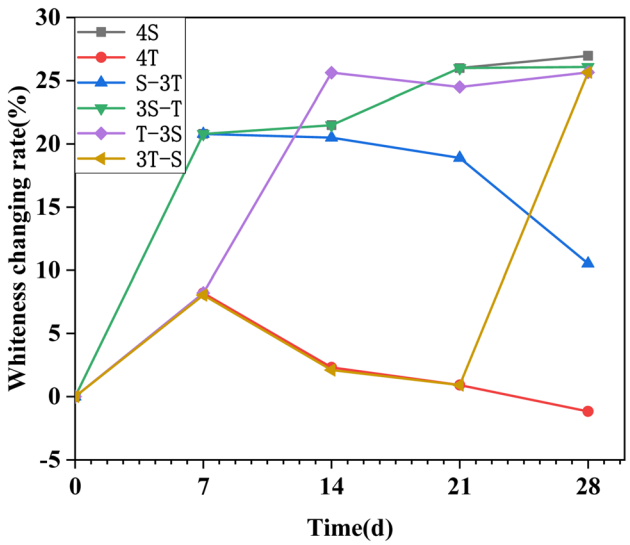

Fig. 7 Whiteness change rate of WUHPC under different paths.

after being soaked in acid rain, the white crystals formed by acid rain peeled off during the carbonization. However, the change of the whiteness was similar between the single or coupling corrosion processes.

3.4 Erosion depth

Fig. 8 shows the erosion depth of WUHPC under different corrosion paths. For acid rain, the erosion depth increased linearly at a rate of 33.0 μm per day, and reached the maximum of 1.85 mm at 56 days. Meanwhile, the corrosion of single carbonation was the slowest at only 0.22 mm. The high diffusion resistance was caused by the compact WUHPC matrix.

However, under the coupling regime, the growth of the erosion depth in the carbonization stage was not negligible. For S-3T and 3S-T, the average erosion rates of carbonization were 7.1 μm per day and 20.0 μm per day, respectively, which were higher than 3.9 μm per day of single carbonization. The results also proved that under the coupling condition, acid rain promoted the erosion of carbonization. On the other hand, during the first acid rain cycle after carbonization, the erosion depth increased faster than in single acid rain, and the effect was mitigated with time.

3.5 Corrosion products and components

To better understand the process of coupling corrosion, the corrosion products were examined by XRD, and the results are shown in Fig. 9. The control group was WUHPC immersed in water as comparison. It was found that the characteristic peaks of C_2S, C_3S, $CaCO_3$ and CH, which existed in the control group, disappeared after acid rain corrosion. When immersed in acid solution, the calcium hydroxide from WUHPC reacted with SO_4^{2+} in solution to form gypsum, and the reaction equation is shown in eqn (3).

$$Ca^{2+} + SO_4^{2-} + 2H_2O \rightarrow CaSO_4 \cdot 2H_2O \quad (3)$$

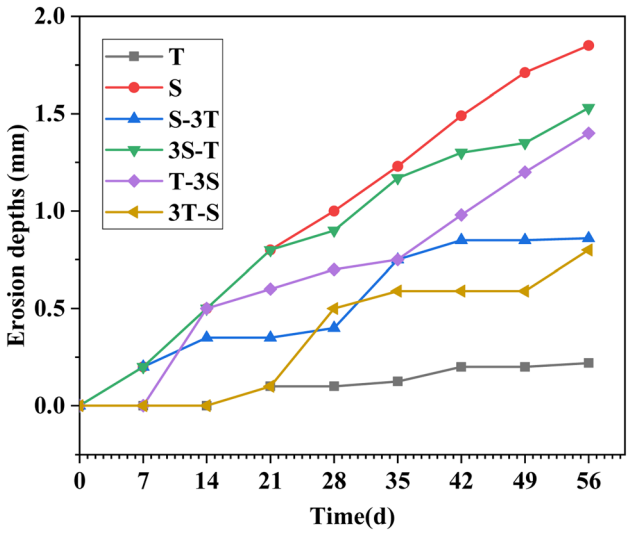

Fig. 8 Erosion depth of WUHPC under different paths.

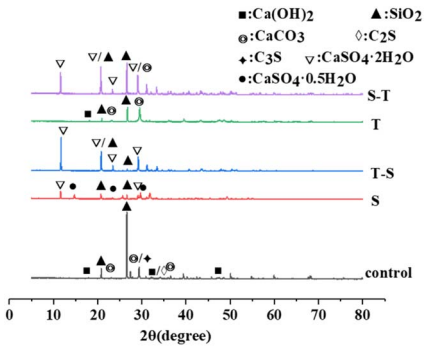

Fig. 9 XRD pattern of erosion products of WUHPC under different paths.

After rapid carbonation, only calcium hydroxide, calcium carbonate, and quartz were detected in WUHPC and the other hydration products disappeared, which indicated that carbonation dissolved the hydration products on the surface of WUHPC. The intense peaks of calcium carbonate were found in samples from acid rain after carbonization (S-T), which confirmed that calcium carbonate was still formed after acid rain soaking. However, calcium carbonate disappeared in the patterns of the reversed process (T-S), indicating that calcium carbonate was dissolved in acid rain solution.

Based on the XRD analysis, gypsum and calcium carbonate are the primary corrosion products in acid rain and carbonization. The contents of the products were further studied by TG-DSC.

The TG-DSC curves of the samples are shown in Fig. 10. Compared to the control group, an exothermic peak existed at 100–200 °C for the sample soaked in acid rain, corresponding to the dehydration of gypsum. The content of gypsum was calculated by eqn (4).

$$M_g = M_w \times \gamma_g/(2 \times \gamma_{H_2O}) \quad (4)$$

where M_g is the mass of gypsum, M_w is the mass loss during the dehydration, γ_g is the molecular weight of gypsum, and γ_{H_2O} is the molecular weight of water.

After calculation, the contents of gypsum in the 4S, S-3T, 3T-S, 3S-T and T-3S samples were determined as 39.26%, 11.10%, 14.44%, 25.83% and 9.37%, respectively. Meanwhile, the 4S sample had no detected gypsum. From the results, it can be seen that the gypsum dosage decreased in the coupling process. This is because the calcium carbonate formed at the early stage blocked some pores on the surface to impede the diffusion of corrosion ions in acid rain. After calcium carbonate was consumed by H^+, the dissolved Ca^{2+} was reacted with SO_4^{2-} to generate gypsum.

3.6 Pore size distribution

Fig. 11 shows the pore size distribution and pore size ratio of WUHPC after corrosion. The pores in concrete were usually divided into gel pores (<0.01 μm), capillary pores (0.01–5 μm) and macropores (>5 μm). As shown in Fig. 11(a), the pore size of WUHPC was concentrated between 0.001–0.1 μm, and

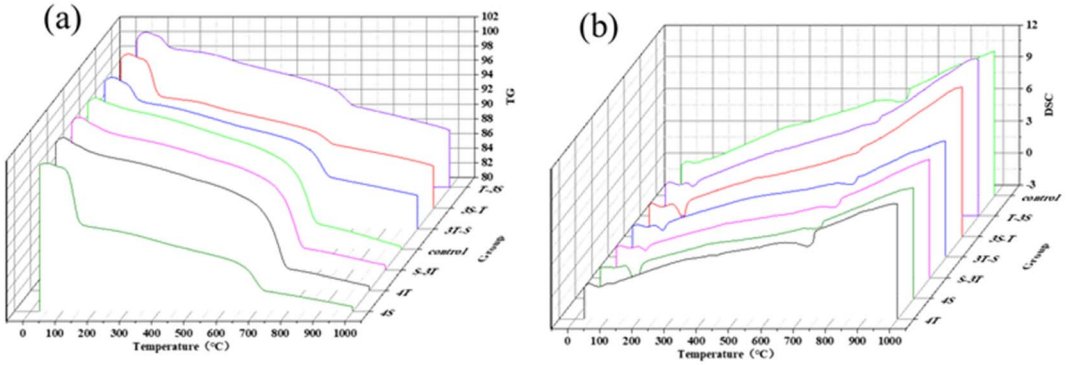

Fig. 10 (a) TG and (b) DSC curves of WUHPC with different corrosion.

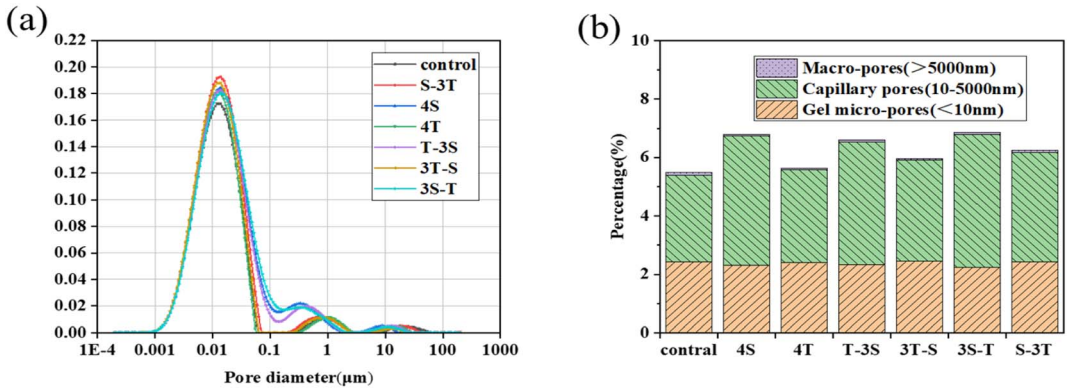

Fig. 11 Effect of different paths on (a) pore size distribution and (b) percentage of porosity.

mainly belonged to gel pores and capillary pores. After acid rain and carbonization, the capillary pores were increased. After single acid rain, the content of the capillary pores increased to 48.8%, while the proportion of macropores and gel pores changed little or decreased, which led to an increase in strength and erosion depth. After single carbonization, the total porosity and capillary pores increased by 2.5% and 7.0%, respectively. Under the coupling regimes, the capillary pores of the S-3T, 3S-T, T-3S and 3T-S samples were increased to 25.9%, 53.2%, 41.5% and 17.1%, respectively. However, the macropores decreased by 0.68%, 27.5%, 14.1% and 56.8%, respectively. The changes of the pore structure in 3S-T and T-3S were equivalent to that of single acid rain erosion, which indicated that the combination of acid rain and carbonization promoted the corrosion of WUHPC in both sides. The pore structure of 3T-S and 3S-T was significantly larger than that of single carbonation.

3.7 Micro-morphology of WUHPC

Fig. 12 shows the SEM diagram of WUHPC under different conditions. For the control sample, the matrix was uniform and dense, with little cracks. However, after carbonization (4T), plenty of small crystal powders were distributed in the matrix, causing some defects. For acid rain erosion (4S), a large amount of rod-like gypsum crystal was formed, crisscrosses into a network and covered the surface, making the surface more loose and brittle. Meanwhile, for the coupling condition (taking S-3T and 3T-S for examples), it was found that larger rod-like gypsum crystals still existed, along with the needle and cluster-formed products in S-3T. However, the number and size of the gypsum products in 3T-S were much smaller. This inferred that the carbonization products compacted the surface of WUHPC, and limited the space for gypsum crystal growth.

The morphology of the erosion products in acid rain at different stages was also observed, and is shown in Fig. 13. When WUHPC was immersed in acid rain solution for the first 1 h (Fig. 13(a)), the corrosion products were complex, including needles, rods and stripe-shaped crystals with different sizes. Then, the large stripe-shaped crystals began to split into small rods with the length of 10–30 μm. By 18 h, there were only needle-like crystals left, forming a petaloid structure, and the shape became more uniform, as shown in Fig. 13(c). With the increasing time, the length of the products decreased and transformed into granular crystals with a particle size of about 1 μm at 54 h. The granular products were loose with weak cementation performance, causing the increase of porosity and spalling of the surface. The concentration of ammonium sulfate solution in acid rain played a decisive role on the change of product size. When the concentration of ammonium sulfate solution increased, the growth orientation

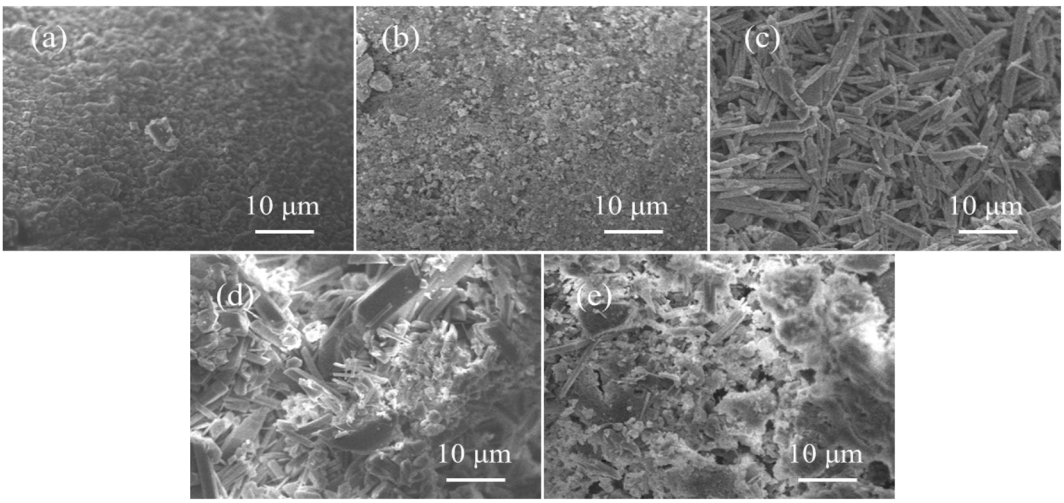

Fig. 12 SEM diagram of WUHPC under different paths: (a) control; (b) 4T; (c) 4S; (d) S-3T; (e) 3T-S.

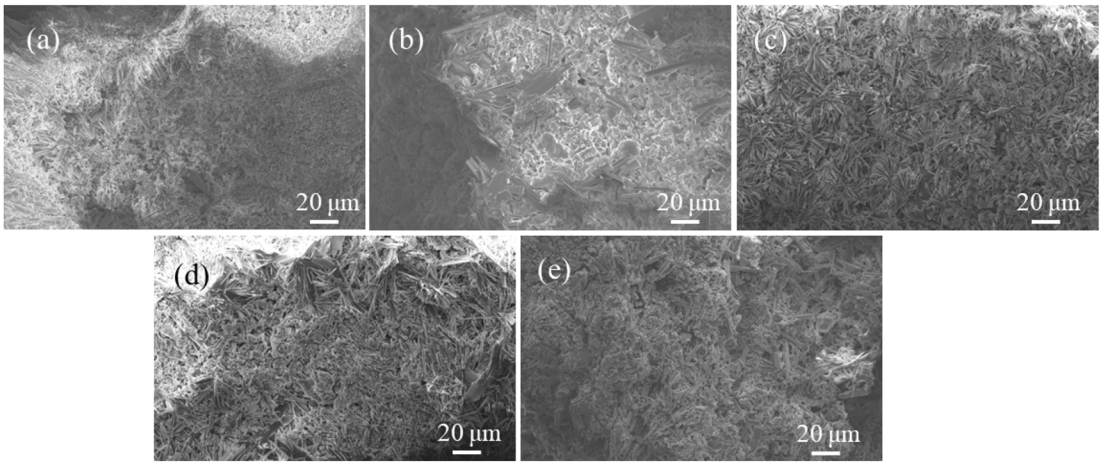

Fig. 13 Morphology changes of the erosion products under different acid rain erosion times: (a) 1 h; (b) 6 h; (c) 18 h; (d) 30 h; (e) 54 h.

of the gypsum crystal changed and the particle size of the crystal changed.[22]

4 Conclusion

The degradation performance and microstructure properties of WUHPC under acid rain and carbonization coupling condition were investigated in this paper. The results demonstrated that WUHPC performed well on weight loss, strength loss and whiteness change under severe corrosion environments, and the coupling condition accelerated the corrosion process.

The weight loss and strength of WUHPC was more affected by acid rain compared to carbonization. The improvement of WUHPC at the early stage (7 days) of acid rain contributed to the precipitation of gypsum crystal, but rapidly deteriorated at the last major cycle. Under the coupling regime, the corrosion rate of carbonization was increased to 7.1 μm per day and 20.0 μm per day, compared to 3.9 μm per day under pure carbonization. The corrosion rate of acid rain after carbonization was also accelerated at the first cycle, and was then mitigated.

Gypsum and calcium carbonate are the primary erosion products in acid rain and carbonization. Under the coupling corrosion process, the first formed carbonate blocked the pores on the surface, hindered the transfer of H^+ and SO_4^{2+} into the matrix, and the dosage of gypsum was decreased. However, the carbonate was quickly consumed by acid solution, leaving more pores and cracks. The products of WUHPC under the action of acid rain were mainly plate-like and needle-like crystals, and most were clustered structures. With the increase of acid rain soaking time, the plate-like and needle-like crystals gradually became shorter and thinner, with part of the needle bars gradually being dissolved into granular crystals, and the bonding properties were lost.

Data availability

Data for this article, including mass change, strength change, corrosion depth, L-NMR and TG-DSC, are available at *RSC Advances* at **https://share.weiyun.com/Q6dwN4jo**.

Author contributions

Huiying Hu: investigation, methodology, writing – original draft. Rui Ma: conceptualization, funding acquisition, writing – review & editing. Ziyang Tian: formal analysis, methodology. Zhidan Rong: conceptualization, resource. Daosheng Sun: supervision.

Conflicts of interest

The authors declare that they have no known competing financial interests or personal relationships that could have appeared to influence the work reported in this paper.

Acknowledgements

This work was supported by the National Natural Science Foundation of China (52208227), Natural Science Foundation for High School of Anhui Province (KJ2021A0625, 2022AH030038), and Overseas Visiting Research Funding Program for Young Key Teachers of Anhui Province (JWFX2023024).

References

1 X. Lu, S. J. Zhang, J. Xing, *et al.*, Progress of Air Pollution Control in China and Its Challenges and Opportunities in the Ecological Civilization Era, *Engineering*, 2020, **6**, 1423–1431.
2 A. M. Vicedo-Cabrera, N. Scovronick, F. Sera, *et al.*, The burden of heat-related mortality attributable to recent human-induced climate change, *Nat. Clim. Change*, 2021, **11**, 492–500.
3 Y. J. Du, N. J. Jiang, S. L. Shen, *et al.*, Experimental investigation of influence of acid rain on leaching and hydraulic characteristics of cement-based solidified/stabilized lead contaminated clay, *J. Hazard. Mater.*, 2012, **225**, 195–201.
4 T. Li, M. Zhan, X. Y. Chen, *et al.*, Study on Carbonization Characteristics and Deterioration Mechanism of Recycled Concrete with Tailings and Polypropylene Fiber, *Polymers*, 2022, **14**, 2758.
5 Y. Li, Y. Q. Su, K. H. Tan, *et al.*, Pore structure and splitting tensile strength of hybrid basalt-polypropylene fiber reinforced concrete subjected to carbonation, *Constr. Build. Mater.*, 2021, **297**, 123779.
6 Y. Z. Zhang, L. Y. Gu and Q. L. Zhang, Durability of manufactured sand concrete in atmospheric acidification environment, *Case Stud. Constr. Mater.*, 2022, **17**, e01613.
7 J. L. Huang, R. X. Chen, Y. Zhou, *et al.*, Molecular design and experiment of ion transport inhibitors towards concrete sustainability, *Cem. Concr. Compos.*, 2022, **133**, 104710.
8 J. K. Zhou, X. D. Chen and S. X. Chen, Durability and service life prediction of GFRP bars embedded in concrete under acid environment, *Nucl. Eng. Des.*, 2011, **241**, 4095–4102.
9 H. J. Li, Z. Q. Yang, J. X. Wen, *et al.*, Service life prediction of ballastless track concrete under the coupling effect of fatigue loads and environmental actions: a review, *J. Sustainable Cem.-Based Mater.*, 2022, **12**, 672–686.
10 R. Sampaio, A. Bastos and M. Ferreira, New Sensors for Monitoring pH and Corrosion of Embedded Steel in Mortars during Sulfuric Acid Attack, *Sensors*, 2022, **22**, 5356.
11 M. Tao, J. Wang, H. T. Zhao, *et al.*, The influence of acid corrosion on dynamic properties and microscopic mechanism of marble, *Geomech. Geophys. Geo-Energy Geo-Resour.*, 2022, **8**, 36.
12 F. L. Jiang, Z. Wang, G. Chen, *et al.*, Experimental study of different admixture effects on the porosity and U(VI) leaching characteristics of uranium tailing solidified bodies in acid rain environments, *J. Radioanal. Nucl. Chem.*, 2021, **329**, 1375–1385.
13 J. M. Ortega, V. E. Garcia-Vera, A. M. Solak, *et al.*, Pore Structure Degradation of Different Cement Mortars Exposed to Sulphuric Acid, *Appl. Sci.*, 2019, **9**, 5297.
14 Y. Zhou, S. S. Zheng, L. Z. Chen, *et al.*, Experimental investigation into the seismic behavior of squat reinforced concrete walls subjected to acid rain erosion, *J. Build. Eng.*, 2021, **44**, 102899.
15 K. Samimi, M. Farahani, M. Pakan, *et al.*, Influence of Pumice and Metakaolin on Compressive Strength and Durability of Concrete in Acidic Media and on Chloride Resistance under Immersion and Tidal Conditions, *Iran. J. Sci. Technol., Trans. Civ. Eng.*, 2022, **46**, 1153–1175.
16 A. Mukhopadhyay and S. Sahoo, Improving corrosion resistance of reinforcement steel rebars exposed to sulphate attack by the use of electroless nickel coatings, *Eur. J. Environ. Civ. Eng.*, 2022, **26**, 5180–5195.
17 Y. Y. Guan and S. S. Zheng, Seismic Behaviors of RC Frame Beam-Column Joints under Acid Rain Circle: A Pilot Experimental Study, *J. Earthq. Eng.*, 2018, **22**, 1008–1026.
18 X. Y. Li, X. T. Yu, Y. Z. Zhao, *et al.*, Effect of initial curing period on the behavior of mortar under sulfate attack, *Constr. Build. Mater.*, 2022, **326**, 126852.
19 X. T. Yu, D. Chen, J. R. Feng, *et al.*, Behavior of mortar exposed to different exposure conditions of sulfate attack, *Ocean Eng.*, 2018, **157**, 1–12.
20 M. Auroy, S. Poyet, P. Le Bescop, *et al.*, Comparison between natural and accelerated carbonation (3% CO_2): impact on mineralogy, microstructure, water retention and cracking, *Cem. Concr. Res.*, 2018, **109**, 64–80.
21 K. Cui, K. K. Liang, J. Chang, *et al.*, Investigation of the macro performance, mechanism, and durability of multiscale steel fiber reinforced low-carbon ecological UHPC, *Constr. Build. Mater.*, 2022, **327**, 126921.
22 G. H. Hou, J. N. Chen, B. Lu, *et al.*, Composition design and pilot study of an advanced energy-saving and low-carbon rankinite clinker, *Cem. Concr. Res.*, 2020, **127**, 105926.
23 B. Esmaeilkhanian, K. H. Khayat and O. H. Wallevik, Mix design approach for low-powder self-consolidating concrete: Eco-SCC-content optimization and performance, *Mater. Struct.*, 2017, **50**, 124.
24 J. L. Parracha, G. Borsoi, R. Veiga, *et al.*, Effects of hygrothermal, UV and SO_2 accelerated ageing on the

durability of ETICS in urban environments, *Build. Environ.*, 2021, **204**, 108151.
25 K. Y. Chen, D. Z. Wu, S. J. Fei, *et al.*, Resistance of blended alkali-activated fly ash-OPC mortar to mild-concentration sulfuric and acetic acid attack, *Environ. Sci. Pollut. Res.*, 2022, **29**, 25694–25708.
26 B. Huang, Z. J. Cheng and J. T. Yao, Experimental study on flexural behavior of rebar concrete beams in industrial building exceeding 50 years, *J. Build. Eng.*, 2022, **46**, 103697.
27 Y. F. Fan, Z. Q. Hu, Y. Z. Zhang, *et al.*, Deterioration of compressive property of concrete under simulated acid rain environment, *Constr. Build. Mater.*, 2010, **24**, 1975–1983.
28 M.-C. Chen, K. Wang and L. Xie, Deterioration mechanism of cementitious materials under acid rain attack, *Eng. Failure Anal.*, 2013, **27**, 272–285.
29 A. Bertron, J. Duchesne and G. Escadeillas, Accelerated tests of hardened cement pastes alteration by organic acids: analysis of the pH effect, *Cem. Concr. Res.*, 2005, **35**, 155–166.
30 Y. Song, S. Zhou, Z. Wang, *et al.*, Mechanism of thaumasite formation in concrete, *J. Wuhan Univ. Technol. Mater. Sci. Ed.*, 2017, **32**, 893–897.
31 X. C. Yan, L. H. Jiang, M. Z. Guo, *et al.*, Evaluation of sulfate resistance of slag contained concrete under steam curing, *Constr. Build. Mater.*, 2019, **195**, 231–237.
32 X. B. Zuo, J. L. Wang, W. Sun, *et al.*, Numerical investigation on gypsum and ettringite formation in cement pastes subjected to sulfate attack, *Comput. Concr.*, 2017, **19**, 19–31.
33 C. Sun, J. K. Chen, J. Zhu, *et al.*, A new diffusion model of sulfate ions in concrete, *Constr. Build. Mater.*, 2013, **39**, 39–45.
34 R. D. Gao, Q. B. Li and S. B. Zhao, Concrete Deterioration Mechanisms under Combined Sulfate Attack and Flexural Loading, *J. Mater. Civ. Eng.*, 2013, **25**, 39–44.
35 J. K. Chen and M. Q. Jiang, Long-term evolution of delayed ettringite and gypsum in Portland cement mortars under sulfate erosion, *Constr. Build. Mater.*, 2009, **23**, 812–816.
36 J. G. Wang, Sulfate attack on hardened cement paste, *Cem. Concr. Res.*, 1994, **24**, 735–742.
37 A. Pavoine, L. Divet and S. Fenouillet, A concrete performance test for delayed ettringite formation: Part I optimisation, *Cem. Concr. Res.*, 2006, **36**, 2138–2143.
38 X. Wang and Z. Pan, Chemical changes and reaction mechanism of hardened cement paste–$(NH_4)_2SO_4$–H_2O system, *Constr. Build. Mater.*, 2017, **152**, 434–443.
39 P. H. R. Borges, J. O. Costa, N. B. Milestone, *et al.*, Carbonation of CH and C–S–H in composite cement pastes containing high amounts of BFS, *Cem. Concr. Res.*, 2010, **40**, 284–292.
40 Q. Pu, L. Jiang, J. Xu, *et al.*, Evolution of pH and chemical composition of pore solution in carbonated concrete, *Constr. Build. Mater.*, 2012, **28**, 519–524.
41 Z. Z. Wang, K. L. Ma, Y. J. Xie, *et al.*, Finite element analysis on properties evolution of slab track FLC under the coupling action of rainfall and fatigue load, *Eng. Struct.*, 2022, **271**, 114919.
42 E. Janowska-Renkas and A. Kaliciak, Impact of Fly Ashes from Combustion in Fluidized Bed Boilers and Siliceous Fly Ashes on Durability of Mortars Exposed to Seawater and Carbonation Process, *Materials*, 2021, **14**, 2345.
43 Y. Peng, X. Meng, F. Song, *et al.*, Experimental study on the corrosion characteristics of concrete exposed to acid water containing aggressive carbon dioxide and sodium sulfate, *Constr. Build. Mater.*, 2022, **321**, 126397.
44 D. Sun, W. Zhang, R. Ma, *et al.*, Mechanical, Permeability, and Photocatalytic Properties of White Ultrahigh-Performance Concrete with Nano-TiO_2, *J. Mater. Civ. Eng.*, 2023, **35**, 04022411.
45 R. Ma, Z. Tian, W. Zhang, *et al.*, Preparation and Color Performance of White Ultra-High-Performance Concrete with Large Fraction of Quaternary Binders, *Materials*, 2022, **15**, 8895.
46 M. Aboukifa and M. A. Moustafa, Reinforcement detailing effects on axial behavior of full-scale UHPC columns, *J. Build. Eng.*, 2022, **49**, 104064.
47 M. G. Sohail, R. Kahraman, N. Al Nuaimi, *et al.*, Durability characteristics of high and ultra-high performance concretes, *J. Build. Eng.*, 2021, **33**, 101669.
48 R. Yu, P. Spiesz and H. J. H. Brouwers, Development of an eco-friendly Ultra-High Performance Concrete (UHPC) with efficient cement and mineral admixtures uses, *Cem. Concr. Compos.*, 2015, **55**, 383–394.
49 L. Liu, Z. He, X. Cai, *et al.*, Application of Low-Field NMR to the Pore Structure of Concrete, *Appl. Magn. Reson.*, 2021, **52**, 15–31.